Since January 2020 Elsevier has created a COVID-19 resource centre with free information in English and Mandarin on the novel coronavirus COVID-19. The COVID-19 resource centre is hosted on Elsevier Connect, the company's public news and information website.

Progress in Biophysics and Molecular Biology 163 (2021) 171–186

Contents lists available at ScienceDirect

Progress in Biophysics and Molecular Biology

journal homepage: www.elsevier.com/locate/pbiomolbio

Targeting SARS-CoV-2 Nsp3 macrodomain structure with insights from human poly(ADP-ribose) glycohydrolase (PARG) structures with inhibitors

Chris A. Brosey [a, *], Jerry H. Houl [a], Panagiotis Katsonis [b], Lakshitha P.F. Balapiti-Modarage [c], Shobanbabu Bommagani [c], Andy Arvai [d], Davide Moiani [a], Albino Bacolla [a], Todd Link [a], Leslie S. Warden [a], Olivier Lichtarge [b], Darin E. Jones [c], Zamal Ahmed [a, **], John A. Tainer [a, e, f, ***]

[a] Department of Molecular and Cellular Oncology, M. D. Anderson Cancer Center, Houston, TX, 77030, USA
[b] Department of Molecular and Human Genetics, Baylor College of Medicine, Houston, TX, 77030, USA
[c] Department of Pharmaceutical Sciences, University of Arkansas for Medical Sciences, Little Rock, AR, 72205, USA
[d] Integrative Structural & Computational Biology, The Scripps Research Institute, La Jolla, CA, 92037, USA
[e] Department of Cancer Biology, M.D. Anderson Cancer Center, Houston, TX, 77030, USA
[f] Molecular Biophysics and Integrated Bioimaging, Lawrence Berkeley National Laboratory, Berkeley, CA, 94720, USA

ARTICLE INFO

Article history:
Received 16 October 2020
Received in revised form
25 January 2021
Accepted 10 February 2021
Available online 23 February 2021

Keywords:
SARS-CoV-2 Nsp3 macrodomain
Poly(ADP-Ribose) glycohydrolase (PARG)
PARG inhibitor (PARGi)
Evolutionary trace (ET)
In silico screening
Drug discovery

ABSTRACT

Arrival of the novel SARS-CoV-2 has launched a worldwide effort to identify both pre-approved and novel therapeutics targeting the viral proteome, highlighting the urgent need for efficient drug discovery strategies. Even with effective vaccines, infection is possible, and at-risk populations would benefit from effective drug compounds that reduce the lethality and lasting damage of COVID-19 infection. The CoV-2 MacroD-like macrodomain (Mac1) is implicated in viral pathogenicity by disrupting host innate immunity through its mono(ADP-ribosyl) hydrolase activity, making it a prime target for antiviral therapy. We therefore solved the structure of CoV-2 Mac1 from non-structural protein 3 (Nsp3) and applied structural and sequence-based genetic tracing, including newly determined *A. pompejana* MacroD2 and GDAP2 amino acid sequences, to compare and contrast CoV-2 Mac1 with the functionally related human DNA-damage signaling factor poly(ADP-ribose) glycohydrolase (PARG). Previously, identified targetable features of the PARG active site allowed us to develop a pharmacologically useful PARG inhibitor (PARGi). Here, we developed a focused chemical library and determined 6 novel PARGi X-ray crystal structures for comparative analysis. We applied this knowledge to discovery of CoV-2 Mac1 inhibitors by combining computation and structural analysis to identify PARGi fragments with potential to bind the distal ribose and adenosyl pockets of the CoV-2 Mac1 active site. Scaffold development of these PARGi fragments has yielded two novel compounds, PARG-345 and PARG-329, that crystallize within the Mac1 active site, providing critical structure-activity data and a pathway for inhibitor optimization. The reported structural findings demonstrate ways to harness our PARGi synthesis and characterization pipeline to develop CoV-2 Mac1 inhibitors targeting the ADP-ribose active site. Together, these structural and computational analyses reveal a path for accelerating development of antiviral therapeutics from pre-existing drug optimization pipelines.

Abbreviations: Severe Acute Respiratory Syndrome, (SARS); nonstructural protein 3, (Nsp3); 2-(N-morpholino)ethanesulfonic acid, (MES); poly(ADP-ribose) glycohydrolase, (PARG); poly(ADP-ribose) polymerase, (PARP); evolutionary trace, (ET); multiple sequence alignment, (MSA); microscale thermophoresis, (MST).

* Corresponding author.
** Corresponding author.
*** Corresponding author. Department of Molecular and Cellular Oncology, M. D. Anderson Cancer Center, Houston, TX, 77030, USA.
E-mail addresses: CABrosey@mdanderson.org (C.A. Brosey), ZAhmed@mdanderson.org (Z. Ahmed), JTainer@mdanderson.org (J.A. Tainer).

https://doi.org/10.1016/j.pbiomolbio.2021.02.002

1. Introduction

As of early 2021, the zoonotic coronavirus disease 2019 (COVID-19) has infected over 100 million people, causing over 2.5 million deaths and imposing worldwide lockdowns (https://coronavirus.jhu.edu/) (Guan et al., 2020; Lam et al., 2020; Zhou et al., 2020). The search for effective antiviral therapies to treat COVID-19 has been broad and varied, ranging from repurposing known FDA-approved drugs to *de novo* fragment-based drug discovery (Omolo et al., 2020; Shyr et al., 2020; Touret et al., 2020). An intermediate option in this arsenal of drug development applies existing inhibitor development pipelines from human disease targets to viral homologues. The CoV-2 MacroD-like macrodomain (Mac1) of non-structural protein 3 (Nsp3) has emerged as an attractive therapeutic target, as macrodomain activity in related coronaviruses has been linked to viral virulence and disruption of innate host immunity (Fehr et al., 2016, 2018; Grunewald et al., 2019). As a candidate for repurposed inhibitor pipelines, CoV-2 Mac1 is functionally related to the key human DNA-damage signaling factor poly(ADP-ribose) glycohydrolase (PARG).

PARG has been the focus of concentrated inhibitor development for cancer, both as a complement to and substitute for clinical PARP inhibitors (PARPi) (Chen and Yu, 2019; Houl et al., 2019; Slade, 2020), which act in part by trapping PARP1 on damaged DNA (Zandarashvili et al., 2020) and by acting synergistically to kill cancer cells with defective homology-directed repair (Syed and Tainer, 2018) or alternative end-joining (Eckelmann et al., 2020). Following DNA damage, PARG reverses the signaling response initiated by PARP1 at ssDNA breaks by hydrolyzing the 'cloud' of poly(ADP-ribose) (PAR) into mono-nucleotide ADP-ribose (ADPr) (Pourfarjam et al., 2020; Slade et al., 2011). The dispersion of the PAR cloud enables subsequent progression of DNA repair at the damage site. Excessive and unresolved PAR depletes NAD^+ and triggers cell death by parthanatos (Brosey et al., 2016; Wang et al., 2011). As a member of the macrodomain family, PARG shares a conserved fold for recognition and chemical hydrolysis of ADP-ribose moieties with CoV-2 Mac1 (Kim et al., 2012; Lambrecht et al., 2015; Rack et al., 2020a).

The largest SARS-CoV-2 non-structural protein, Nsp3, contains three macrodomain folds: Mac1 and two SUD-M-like domains (SUD-M-N, SUD-M-C) (Alhammad and Fehr, 2020; Frick et al., 2020). The CoV-2 Mac1 domain possesses mono(ADP-ribosyl) hydrolase activity *in vitro*, reversing PARP14 modifications (Rack et al., 2020b) and is proposed to remove single ADP-ribose modifications from host protein substrates in cells (Alhammad and Fehr, 2020; Lin et al., 2020; Rack et al., 2020b). Critically, catalytic inactivation of coronavirus macrodomains attenuates viral pathogenesis in mice and restores interferon responses (Abraham et al., 2020; Fehr et al., 2015, 2016; McPherson et al., 2017). Viral macrodomains are believed to counter or hijack host immunity by reversing the mono(ADP-ribosyl) modifications generated by host PARP14 enzymes, thereby interfering with interferon production (Grunewald et al., 2019) and altering STAT1 regulation (Iwata et al., 2016), a possible link to the damaging and deadly Cytokine Storm Syndrome observed in severe COVID-19 cases (Claverie, 2020). These observations implicate CoV-2 Mac1 as a critical target for antiviral therapy, and a variety of screening efforts are underway to discover fragment binders as leads to potential inhibitors (Fraser, 2020).

Given the conserved macrodomain fold shared between CoV-2 Mac1 and PARG, we investigated how our current PARGi libraries and pharmacology could be interrogated for accelerated inhibitor development against CoV-2 Mac1. We crystallized and determined a 1.45 Å-structure of the CoV-2 Mac1 domain, identifying a bound MES molecule with similarities to our NCI JA2131 lead PARG inhibitor in the distal ribose active site. We also determined 6 novel PARGi X-ray crystal structures from our focused JA2131 derivative library in order to probe the conformational diversity available to PARGi ligands engaging the PARG macrodomain active site. By using evolutionary trace data and including newly determined *A. pompejana* MacroD2 and GDAP2 amino acid sequences, we identified functionally significant active site residues shared between CoV-2 Mac1 and PARG-like macrodomains. Computational screening and triaging of our PARGi libraries against CoV-2 Mac1 revealed candidate PARGi fragments targeting these conserved residues in the adenosyl and distal ribose pockets. These PARGi fragments were rationally reoptimized to create a new panel of CoV-2 Mac1 inhibitors targeting both active site pockets. These efforts yielded two novel compounds, PARG-345 and PARG-329, that crystallize in the Mac1 active site and provide critical structural information for optimizing the affinity and inhibitory activity of these scaffold designs using our existing ligand characterization pipelines. The structure of CoV-2 Mac1 in combination with specific inhibitors will open the door to defining its cellular protein targets and biological activity for foundational insights into SARS-CoV-2 pathogenesis. Our approach provides a generalizable framework for leveraging pre-existing inhibitor pipelines from human homologues as a strategy for antiviral drug development.

2. Materials and methods

2.1. CoV-2 Mac1 expression, purification, and validation

The CoV-2 Mac1 sequence (Fig. S1) was subcloned into a pET-30a(+) vector with a 6X-Histidine fusion tag and 3C protease cleavage site by Genscript. CoV-2 Mac1 was recombinantly expressed in *E. coli* Rosetta 2(DE3) cells using auto induction media at 20 °C. Frozen cell pellets were resuspended on ice in lysis buffer (50 mM HEPES, pH 8.0, 500 mM NaCl, 10% glycerol, 0.5 mM TCEP) supplemented with 1 mM PMSF, 1 mg/ml lysozyme, and 10 μg/ml DNase I. The suspension was lysed via 3 passes through an Avestin EmulsiFlex C5 Cell disruptor and spun at 18,000 rpm in a Sorvall SS-34 rotor for 60 min at 4 °C. The supernatant was loaded onto a 5-ml GE HisTrap column, washed with 10 column volumes (CV) of lysis buffer, 5 CV of lysis buffer plus 25 mM imidazole, and eluted with lysis buffer plus 300 mM imidazole. Fractions containing the His_6-CoV-2 Mac1 were treated with PreScission protease and dialyzed overnight in 2 L of lysis buffer at 4 °C. Subtractive chromatography was performed with the 5-ml GE HisTrap column, and the cleaved CoV-2 Mac1 product was eluted with lysis buffer plus 25 mM imidazole. The CoV-2 Mac1 was furthered purified on a Superdex 75 16/60 gel filtration column using 20 mM HEPES, pH 7.5, 200 mM NaCl, and 0.5 mM TCEP. Fractions containing protein were pooled, flash frozen in liquid nitrogen, and stored at −80 °C.

Purified CoV-2 Mac1 was assayed for its ability to bind ADP-ribose using isothermal titration calorimetry (ITC) with a PEAQ-ITC (Malvern Panalytical). Buffer-matched ADP-ribose stock (1 mM in 25 mM HEPES, pH 7.5, 150 mM NaCl) was titrated into buffer or 40–50 μM CoV-2 Mac1 at 25 °C in 19 2-μL injections (4 s each) spaced at 150 s and stirred at 750 rpm. ITC thermograms were baseline corrected and integrated, followed by subtraction of background heats from the ligand-to-buffer titration in MicroCal PEAQ-ITC Analysis Software. The same software was used to determine thermodynamic parameters.

2.2. CoV-2 Mac1 crystallization and structure determination

Crystals of CoV-2 Nsp3 Mac1 were grown by the hanging-drop vapor diffusion method in 70% saturated ammonium sulfate, 0.4% BME, 200 mM Imidazole/Malate pH 7.4, and 50 mM MES pH 6.0–8.6. Protein and mother liquor were mixed in a 1:1 ratio in 2 μL

drops and equilibrated at 15 °C. Crystals grew to full size in approximately five days. Crystals were harvested, briefly exchanged into cryoprotectant buffer (20% glycerol, i.e. 4 μL reservoir mixed with 1 μL glycerol), and flash cooled in liquid nitrogen for the native macrodomain structure. For PARG-329 and PARG-345 complexes, crystals were soaked in 10 mM (329) or 11.5 mM (345) drug with 60% ammonium sulfate, 0.4% BME, 200 mM imidazole/malate, pH 7.8 (329) or pH 8.2 (345) for 5 h prior to flash freezing in soak solution supplemented with 20% glycerol.

X-ray diffraction data were collected at SSRL beamlines 9-2 and 12–2, and datasets were processed with XDS (Kabsch, 2010). The structure was solved with molecular replacement with Phaser, using PDB: 6YWM, chain A as a search model. The structure was built with alternating rounds of refinement in Phenix (Liebschner et al., 2019) and manual fitting with Coot (Emsley and Cowtan, 2004). Final coordinates for all CoV-2 Mac1 structures have been deposited in the Protein Data Bank [MES (7KG3), PARG-329 (7KXB), PARG-345 (7LG7)]. C_α RMSD values were calculated in Chimera (Pettersen et al., 2004).

2.3. Synthesis of methylxanthine PARGi derivatives and Mac1 MES-derived inhibitors

The lead NCI library compound JA2131 (NSC99667) was previously identified and characterized as a PARG inhibitor *in vitro* and in cells (Houl et al., 2019). General approaches for derivatization of the JA2131 pharmacophore are as follows.

A general scheme for the preparation of N7-substituted methylxanthine PARGi **2** is shown in Scheme 1 (Bertrand et al., 2014). Commercially available theophylline **1** is treated with a variety of alkyl halides in the presence of potassium carbonate and affords N7-substituted methylxanthine PARGi **2** analogues in good yield and purity after chromatography.

The general synthesis of C8-substitued methylxanthine PARGi derivatives **5** and N7, C8-disubstitued methylxanthine PARGi derivatives **6** is shown in Scheme 2 (Hisham et al., 2019). Nitrosoation of the commercially available aminouracil **3** followed by reduction and condensation with carbon disulfide resulted in the formation of the thioxanthine **4** after chromatographic purification. The treatment of thioxanthine **4** with alkyl halides in a basic aqueous solution yielded the desired PARGi derivatives **5** as a single regioisomer. PARGi derivatives **5** were further elaborated to N7, C8-disubstitued methylxanthine PARGi derivatives **6** by treatment with potassium carbonate and an appropriate alkyl halide. A detailed description of these syntheses is provided in the Supplemental Experimental Methods.

2.4. PARG purification and crystallization

The human PARG catalytic domain (residues 448–976) was recombinantly expressed and purified as described (Houl et al., 2019). Purified PARG was also crystallized as described (Houl et al., 2019; Tucker et al., 2012) by the hanging-drop vapor diffusion method in 0.1 M PCTP (Sodium propionate, Sodium cacodylate trihydrate, Bis-Tris propane), pH 7.5, 0.2 M $AmSO_4$, 18–23% PEG3350. PCTP buffer was obtained from Molecular Dimensions. Seeding was used to improve crystal yield and morphology (1.5 μL 7.5 mg/mL protein, 0.5 μL seed stock, 1.0 μL mother liquor). Crystals were harvested and soaked in 1–10 mM PARGi (prepared from 50 mM stocks in DMSO) for 1–2 h at 22 °C in soak/cryoprotectant buffer (0.1 M PCTP, pH 7.5, 0.1 M NaCl, 0.15 M $MgCl_2$, 26% PEG3350, 2.5% glycerol), then flash cooled in liquid nitrogen for data collection. For PARG-131, PARG protein was mixed with 1–10 mM inhibitor and co-crystallized, resulting in a more primitive spacegroup ($P12_11$) relative to the soaked, native crystals ($P2_12_12_1$). PARG-131 co-crystals were briefly soaked in cryoprotectant prior to flash cooling for data collection.

2.5. PARGi structure determination

X-ray diffraction data were collected at Stanford Radiation Lightsource (SSRL) beamlines 9–2 and 12–2 (Russi et al., 2016; Soltis et al., 2008), National Synchrotron Light Source II (NSLS-II) beamlines 17-ID-1 (AMX) and 17-ID-2 (FMX), and Advanced Photon Source (APS) beamline 24-ID-C. X-ray data diffracted to 1.43–1.96 Å resolution and were processed with XDS (Kabsch, 2010) and the CCP4i suite (Winn et al., 2011). Structures with PARGi were determined by molecular replacement using unliganded PARG (PDB: 4B1G) as a search model in Phaser (Bunkoczi et al., 2013). PARGi structures were iteratively built using COOT (Emsley and Cowtan, 2004) and refined in Phenix (Liebschner et al., 2019). Ligand restraints were prepared with eLBOW (Moriarty et al., 2009). Polder difference maps were calculated in Phenix to validate PARGi ligand placement (Liebschner et al., 2017). Molecular images were generated with PyMOL (The PyMOL Molecular Graphics System, Version 2.0, Schrödinger, LLC). Final coordinates of PARGi complexes have been deposited in the Protein Data Bank [PARG-002 (7KG1), PARG-061 (7KG8), PARG-119 (7KFP), PARG-131 (7KG0), PARG-292 (7KG7), PARG-322 (7KG6)].

2.6. Identification of the MacroD2 and GDAP2 genes in the extremophile Alvinella pompejana

We used the *de novo* assembler SoapDeNovo2 on a library of short reads generated from *A. pompejana* samples collected during past expeditions (2003–2004) in the East Pacific Rise (Shin et al., 2009) to obtain a partial assembly of the annelid genome. To the scaffolds obtained we added a curated set of ESTs (Holder et al., 2013), from which we selected a training set of full-length transcripts to conduct a gene prediction analysis using AUGUSTUS (Stanke and Morgenstern, 2005). The human UNIPROT entries A1Z1Q3 for MACROD2 and Q9NXN4 for GDAP2 were then used to query the augustus.gtf prediction dataset using blastp. We then used bedtools (version 2.25.0) to extract the nucleotide sequences from the scaffolds and the amino acid sequences from the augustus.aa prediction dataset. The top blastp scores were 3e-85 for MACROD2 and 9e-168 for GDAP2. For GDAP2 we found support from both the genome assembly and from a full-length EST. The *A. pompejana* protein sequences were further used in a blastp search against the Protostomia clade to verify that top homology was indeed with the same human gene bait. *A. pompejana* MacroD2 and GDAP2 amino acid sequences are reported in Table S2 and have been deposited with GenBank (MW349132 and MW383972).

2.7. Macrodomain phylogeny analysis

Macrodomain sequences were selected to represent the six macrodomain subfamilies and were partially based on the listing

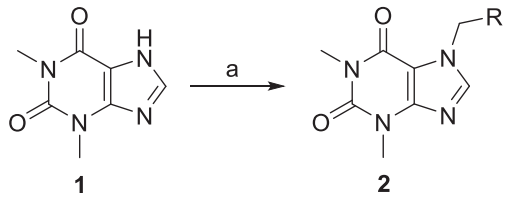

1 2

Scheme 1. Preparation of N7-substitued methylxanthine PARGi derivatives. Reagents and conditions: (a) alkyl halide, K_2CO_3, DMF, 90 °C, 12 h.

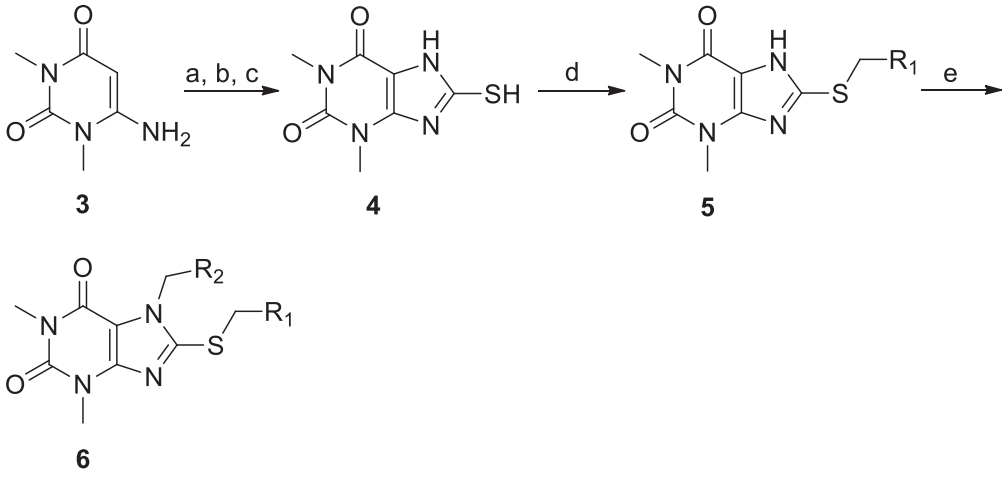

Scheme 2. Preparation of C8-substitued methylxanthine PARGi derivatives **5** and N7, C8-disubstitued methylxanthine PARGi derivatives **6**. Reagents and conditions: (a) $NaNO_2$, 50% AcOH, RT, 2 h; (b) Pd/C, H_2, Ethanol, RT, 2 h; (c) CS_2, DMF, reflux, 2 h; (d) Alkyl halide, 1% aq. NaOH, RT. (e) alkyl halide, K_2CO_3, DMF, 90 °C, 12 h.

described in (Rack et al., 2016). Macrodomain sequences were extracted from each gene ID (Table S1) and aligned using the structure- and sequence-informed Espresso pipeline of the T-Coffee multiple sequence alignment web server (Armougom et al., 2006; Notredame et al., 2000). A phylogenetic tree was calculated from the resulting sequence alignment as follows. The evolutionary history was inferred using the Neighbor-Joining method (Saitou and Nei, 1987). The bootstrap consensus tree inferred from 500 replicates was taken to represent the evolutionary history of the taxa analyzed (Felsenstein, 1985). Branches corresponding to partitions reproduced in less than 50% bootstrap replicates were collapsed. The evolutionary distances were computed using the p-distance method (Nei, 2000) and are in the units of the number of amino acid differences per site. This analysis involved 48 amino acid sequences. All ambiguous positions were removed for each sequence pair (pairwise deletion option). There were a total of 7365 positions in the final dataset. Phylogenetic analyses were conducted in MEGA X (Kumar et al., 2018; Stecher et al., 2020).

2.8. Evolutionary trace analysis

Protein-specific evolutionary traces (ET) were constructed for CoV-2 Nsp3 (sequence obtained from the NC_045512.2 genome) and human PARG (NP_003622 sequence) as described in (Mihalek et al., 2004). The homologous sequences for each trace were obtained by BLAST using blastall 2.2.15 (Altschul et al., 1997) and the NCBI nr, UniRef90, and Uniref100 databases (Pruitt et al., 2007; Suzek et al., 2015). The homologous sequences were automatically selected to represent different phylogenetic distances to the sequence of interest while minimizing alignment gaps. The sequences were aligned using MUSCLE (Edgar, 2004). The resulting evolutionary trace ranks were mapped onto the PDB structures: 6W02 (CoV-2 Mac1) and 4B1G (human PARG), respectively, using the PyETV plugin (Lua and Lichtarge, 2010). Macrodomain-specific evolutionary traces were constructed for the greater macrodomain family using the structure-informed multiple sequence alignment (MSA) from curated macrodomain subfamilies (Section 2.6, Table S1). ET values from this broader MSA comparison were mapped to CoV-2 Mac1 and PARG structures, assuming each respectively as the reference sequence for the ET analysis.

2.9. Virtual screening of the PARGi library against COV-2 Mac1

The CoV-2 Mac1 crystal structure with MES exhibits a more open active site relative to the published unliganded (PDB: 6WEY) and (ADP-ribose)-bound (PDB: 6W02) structures and was thus selected as a target for virtual screening. Specifically, the CoV-2 Mac-1 MES structure rotates the F156 phenyl side chain upright to make a π-π stacking interaction with the adenosyl pocket and includes a larger opening between Loops 1 and 2. Waters and the MES ligand were removed, and the structure was minimized using Schrödinger's Protein Preparation wizard (Schrödinger Suite, 2019–2 with Epik, Impact, and Prime, Schrödinger, LLC, New York, NY, 2019). The docking grid was focused on the center of the ADP-ribose pocket (Pro 125) with a 15 Å-cubic box, excluding ligands longer than 20 Å.

Structure data files (SDF) for the 300-compound library of JA2131 PARGi derivatives were extracted from SMILES strings and prepared for docking in Maestro with LigPrep (Schrödinger Suite, 2019–2). The SDF for the control ADP-ribose ligand was retrieved from PubChem (https://pubchem.ncbi.nlm.nih.gov) and also prepared with LigPrep. Virtual high-throughput screening of the PARGi library against the CoV-2 Mac1 target was carried out in Maestro with flexible ligand docking in both standard (SP) and extra-precision modes (XP). MM-GBSA binding energies (ΔG) were calculated for each pose and used to rank the docking results. Poses from the XP screening returned highly variable and unrealistically compacted ligand geometries, suggesting an artifact from the more stringent scoring function. In contrast, MM-GBSA ranked poses from the SP screening returned more consistent and realistic ligand conformations. Thus, the top 20 MM-GBSA ranked poses from the SP screening protocol were selected for further analysis. This approach was repeated with rationally designed Mac1 inhibitors to generate poses for CoV-2 Mac1 binding and to rank these compounds against the PARGi library. Docking poses were visualized and analyzed with PyMOL (The PyMOL Molecular Graphics System, Version 2.0 Schrödinger, LLC) and Chimera (Pettersen et al., 2004). Computational suites were accessed through the SBGrid Consortium (Morin et al., 2013).

2.10. CoV-2 Mac1 MST and ITC binding affinity measurements

MST measurements followed the framework outlined by (Seidel et al., 2013). Purified CoV-2 Mac1 was labeled with Atto488 NHS-

ester (ATTO-TEC) according to the manufacturer's protocol with labeling efficiency 1:1 protein-to-dye ratio. Labeled CoV-2-Mac1 (200 nM) or a combination of labeled (100 nM) and unlabeled (400 nM) CoV-2 Mac1 was combined with 0.01–2.5 mM ADP-ribose, PARG-329, or PARG-345 in MST buffer (10 mM HEPES, pH 7.5, 150 mM NaCl, 0.05% Surfactant P20, GE Healthcare; 5% DMSO was included for drug titrations), incubated for 10–15 min at room temperature, and loaded into standard silica capillaries (NanoTemper). Microscale thermophoresis (MST) measurements were acquired on a Monolith NT.115 system (NanoTemper) at 25 °C with 10–20% LED power and 40% (ADP-ribose) or 60% (PARG-329, PARG-345) infrared excitation for 20–30 s with 5-s equilibration and recovery periods. Data were analyzed with Nano Temper analysis software and displayed with Graphpad Prism 8.

ITC measurements were performed as described above with a PEAQ-ITC instrument using a cell concentration of DMSO-matched 50 μM CoV-2 Mac1 with 3 mM drug in the syringe (25 mM HEPES, pH 7.5, 150 mM NaCl, 6% DMSO). Data were analyzed with the MicroCal PEAQ-ITC Analysis Software.

3. Results

3.1. CoV-2 macrodomain 1 (Mac1) crystallizes with a PARGi template fragment in its active site

To develop tools for PARGi repurposing, we purified and crystallized CoV-2 Mac1, obtaining a 1.45 Å structure (Fig. 1). The purified domain engages the native mono-nucleotide ADP-ribose ligand at a dissociation constant of K_d ~10–12 μM, consistent with previously reported values (Fig. 1A, Table 1) (Frick et al., 2020). Examination of the CoV-2 Mac1 crystal structure reveals a canonical macrodomain fold with a molecule of MES captured within the distal ribose binding site, consistent with other recently reported structures of the CoV-2 macrodomain (Michalska et al., 2020). The Mac1 tertiary fold is nearly identical to the reported apo (C_α RMSD 0.386 Å, PDB: 6WEN), ADPr-bound (0.361 Å, PDB: 6W02), and MES-bound Mac1 structures (0.366 Å, PDB: 6WCF; 0.251 Å, PDB: 6YWM).

The MES ligand is coordinated by hydrogen bonding from N40 of Loop 1 to the morpholine oxygen and by Loop 2 main chain contacts to the sulfonic acid (Fig. 1B). These interactions resemble those made by CoV-2 Mac1 to the β-phosphate and distal ribose of ADP-ribose (Fig. 2B), suggesting that the MES fragment could serve as a template for inhibitor development. Notably, our previously published methylxanthine PARGi JA2131 (Houl et al., 2019) possesses a morpholine extension that could provide a ready-made template for CoV-2 Mac1 inhibitor development (Fig. 4A), offering impetus for a repurposing strategy.

3.2. Phylogenetic analysis assigns CoV-2 Mac1 to the MacroD subfamily

Prior to applying our PARGi library to CoV-2 Mac1 inhibitor development, we created phylogenetic and evolutionary analyses of these two systems to evaluate the similarity of their active sites. To this end, we constructed a phylogenetic tree of the macrodomain family, based upon a sequence- and structure-informed alignment of curated eukaryotic, bacterial, and viral macrodomain sequences from the six macrodomain subfamilies (Fig. 2A, Table S1, Table S2). Consistent with their mono(ADP-ribosyl) hydrolase activity, the betacoronavirus Mac1 domains are most closely related to the MacroD subfamily. Notably, the closest human homologues to these viral macrodomains are the N-terminal macrodomains (Mac1) of PARP9 and PARP14. PARP9 and PARP14 activities are implicated in regulation of macrophage activation (Iwata et al., 2016) and promotion of interferon responses in cells (Caprara et al., 2018; Zhang et al., 2015). The high degree of similarity between the PARP macrodomains and CoV-2 Mac1 could point to molecular mimicry as a mechanism enabling CoV-2 manipulation of host cell immune responses.

The PARG macrodomain subfamily associates to a separate phylogenetic branch relative to the MacroD subfamily and CoV-2 Mac1. In addition to the macrodomain core, PARG enzymes feature an N-terminal accessory domain and small C-terminal helical extension. Mammalian PARG macrodomains contain a unique β-hairpin insert which forms a 'tyrosine clasp' (Y795 in humans) at the ADP-ribose active site that makes contacts with the adenine ring and O5′ and O1A of the α-phosphate (Kim et al., 2012) (Fig. 2B). These structural distinctions are presumed to support PARG's ability to recognize and hydrolyze the O-glycosidic bond of poly (ADP-ribose) substrates.

3.3. COV-2 Mac1 and human PARG macrodomains share critical adenosyl and ribose residues

While COV-2 Mac1 and human PARG occupy phylogenetically distinct branches within the macrodomain family, their active sites retain shared architectural elements which could support PARGi repurposing (Fig. 2B). Visual inspection of these domains in complex with ADP-ribose reveals a conserved aromatic interaction in the adenine binding pocket (F156, F902) and hydrogen bond contacts to N5 of the adenine ring (D22, E727). The canonical Loop 2 exhibits main chain hydrogen bond interactions to α- and β-phosphates of the substrate. The opposing distal ribose pocket is framed by F132/F875 and coordinates the 2′-OH and 3′-OH groups of the distal ribose through hydrogen bond contacts with Loop 1. The preference for main chain coordination in the CoV-2 Mac1 Loop 1 over PARG's selective side chain contacts points to the distinct substrates and chemistry executed by each domain.

In order to rank and prioritize active site regions and residues for computational PARGi screening, we performed Evolutionary Trace (ET) analyses for CoV-2 Mac1 and PARG (Lichtarge et al., 1996; Mihalek et al., 2004). We initially collected homologous sequences for each full-length protein, producing two non-overlapping trees unique to PARG and viral CoV-2 Nsp3 proteins, respectively. The ET analysis of these protein-specific trees prioritizes the active sites of CoV-2 Mac1 and PARG as the location of greatest functional importance within each protein fold (Fig. 3A). Inspection of viral Nsp3 ET values across the macrodomain sequence highlights F156 of the adenosyl binding site (F360 in full-length Nsp3) as a region of relative increased variability within the adenosyl and distal ribose sites (Fig. 3B). The uniqueness of phenylalanine in this position has been noted in other viral macrodomain sequence alignments (Alhammad and Fehr, 2020; Frick et al., 2020; Michalska et al., 2020) and could have functional implications for engaging host cell substrates.

We next assessed the evolutionary importance of active site residues across the greater macrodomain family, represented by our curated, structure-aligned macrodomain sequences used in the phylogenetic analysis (Fig. 2C, Table S1). The resulting ET scores were also projected onto the CoV-2 Mac1 and PARG macrodomain structures (Fig. 2C). This broader analysis across multiple macrodomain subfamilies shows more diffuse ET signal across the active sites. However, residues that contribute side-chain specific contacts to ADP-ribose (noted earlier in structural comparison of the active sites) retain high ET values: F156, D22, N40 (CoV-2 Mac1) and F902, E727, N740, N869, Y795, E756 (PARG). Contacts mediated by main-chain interactions, such as Loops 1 and 2 at the distal ribose, are more likely to exhibit diminished ET values. Interestingly, the ET ranking of CoV-2 F156 is now increased when eukaryotic macrodomains are included in the analysis, reflecting the conservation of

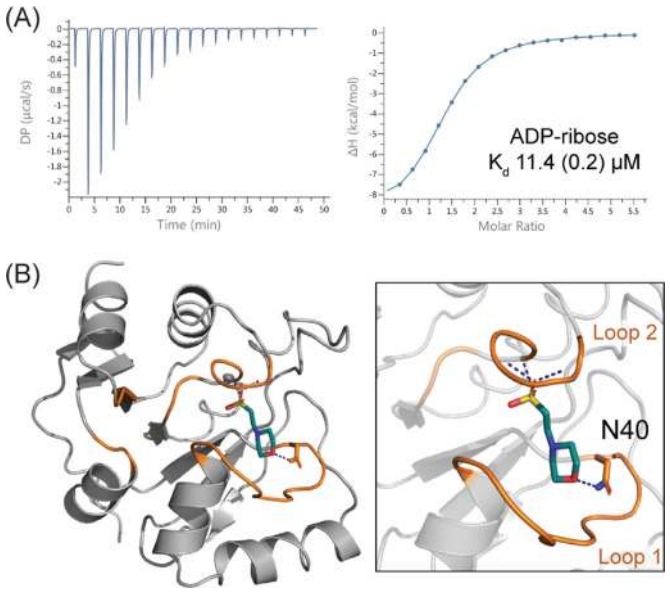

Fig. 1. The CoV-2 Mac1 X-ray crystal structure captures a PARGi template fragment. (A) Purified CoV-2 Mac1 binds to ADP-ribose with the expected affinity by ITC (see also Table 1). Results are representative of 3 independent experiments. (B) Crystal structure of CoV-2 Mac1 with a MES buffer molecule occupying the distal ribose binding site. MES hydrogen bonds with conserved N40 and Loop 2 main chain atoms.

Table 1
CoV-2 Nsp3 Mac1 ITC Binding Parameters. Fit errors are in parentheses.

N	1.29 (0.006)
Kd (μM)	11.6 (0.2)
ΔH (kcal/mol)	−9.18 (0.2)
-TΔS (kcal/mol)	2.43
ΔG (kcal/mol)	−6.74

this residue among MacroD domains. Overall, the ET analysis supports selective inhibitor targeting at F156, D22, and N40 and would prioritize PARGi that engage these residues.

3.4. Virtual screening identifies candidate PARGi fragments for engaging COV-2 Mac1

We generated a JA2131 derivative library of over 300 compounds as part of our PARGi optimization pipeline, incorporating a variety of substitutions at the N3, N7, and C8 positions of the methylxanthine scaffold (Fig. 4). We tested a focused set by determining their X-ray crystal structures bound to PARG (Table S3, Fig. S2). While JA2131 anchors compactly into the adenosyl pocket of the PARG active site, aromatically engaging F902 and Y795 (Fig. 4A), other members of the derivative library exhibit more varied and elongated conformations that would be more adaptable to the extended active site conformations observed for ADP-ribose (Fig. 4B, Fig. S2). The absence of a tyrosine clasp in CoV-2 Mac1 is also expected to increase conformational accessibility to the active site.

To identify candidate PARGi capable of engaging the CoV-2 Mac1 active site, we performed an *in silico* screen using the Maestro suite of Schrodinger to prepare and dock our PARGi ligand library. We selected our own CoV-2 Mac1 crystal structure as a screening target, as it presented a more open, accessible active site conformation compared to crystal structures of unliganded and (ADP-ribose)-bound domains. Binding energies (ΔG) were calculated for the top docked poses using the MM-GBSA method, and these energies were used to rank and extract the top twenty docked complexes (Table 2). As a control, ADP-ribose was included in the docking and was successfully captured in the MM-GBSA ranking strategy. The top-scoring Mac1-ADP-ribose complex effectively captures the ligand binding orientation of the crystal structure (Fig. S3A), placing the adenosyl and distal ribose groups in their respective pockets and aligning the pyrophosphate linker with Loops 1 and 2. The selected APDr poses exhibit rotational variability among the adenosyl and distal ribose groups, but maintain the overall ligand binding path.

Visual inspection of the top twenty docked PARGi complexes reveals two clusters of poses. The first is enriched for C8 phenyl and morpholine derivatives that anchor into the distal ribose site (Fig. 5A). A second, smaller cluster, which contains the top two PARGi poses, anchors the methylxanthine head into the adenine pocket. Inspection of individual poses highlights contacts between the Loop 2 main chain and the conserved N40 of the distal ribose site, similar to those observed for the crystallographic MES ligand (Fig. 1B). Notably, neither compound cluster fully bridges and engages both pockets of the active site, suggesting that extension of the JA2131 scaffold could be required to adapt these derivatives to CoV-2 Mac1. Nonetheless, the virtual 'triaging' provided by these results identifies PARGi fragment templates likely to be most useful in CoV-2 Mac1 inhibitor design.

3.5. Rational design and modeling of COV-2 Mac1 inhibitors based upon PARGi fragments

Direct MST and ITC affinity measurements between purified CoV-2 Mac1 and top PARGi candidates from the *in silico* screen revealed an absence of binding (data not shown), supporting a rationale for reconfiguring and elongating PARGi fragments to target both adenosyl and ribose pockets of the CoV-2 Mac1 active site. These designs incorporate the 2-morpholinoethanesulfonyl moiety, the major fragment of MES, into the linker allowing the sulfone functional group to act as a bioisosteric replacement of ADPr phosphate groups in order to leverage the Loop 2 backbone contacts observed in the crystal structure and *in silico* screening (Table S4) (Elliott et al., 2012). To assess the ability of these first-generation CoV-2-specific inhibitors to bridge the ADP-ribose binding site, we computationally docked these ligands into the active site and ranked the resulting complexes in the context of the PARGi *in silico* results. Only poses for MES8-2 and MES8-4 were returned among the top docking results (Fig. S3B). This suggests that inclusion of the carbonyl functionality of the acyl sulfonamide increases the C—N—S bond angle ~10° and aids in optimally positioning the bridging sulfone to engage with Loop 2 (Fig. 5C, Table S4). The resulting model of the macrodomain/inhibitor complex for MES8-4 captures the ligand fully extended across both pockets of the active site, engaging conserved N40 with its morpholine group, the Loop 2 main chain with the bridging sulfone, and a novel I23 main chain contact in the adenosyl pocket with the methylxanthine head. The insights gained from these computational assessments prioritized these novel CoV-2 Mac1 ligands for synthesis and testing in our inhibitor development pipeline.

3.6. Optimized MES8-4 (PARG-345) and PARG-329 engage the CoV-2 Mac1 active site

Using the virtual screening results as a guide, we synthesized a panel of MES7 and MES8 derivatives for binding assessment and crystallization with CoV-2 Mac1. As predicted, N7 variations of the MESi scaffold (Table S4) did not engage the Mac1 domain (data not shown). However, MES8-4 (PARG-345) and PARG-329, a variant of

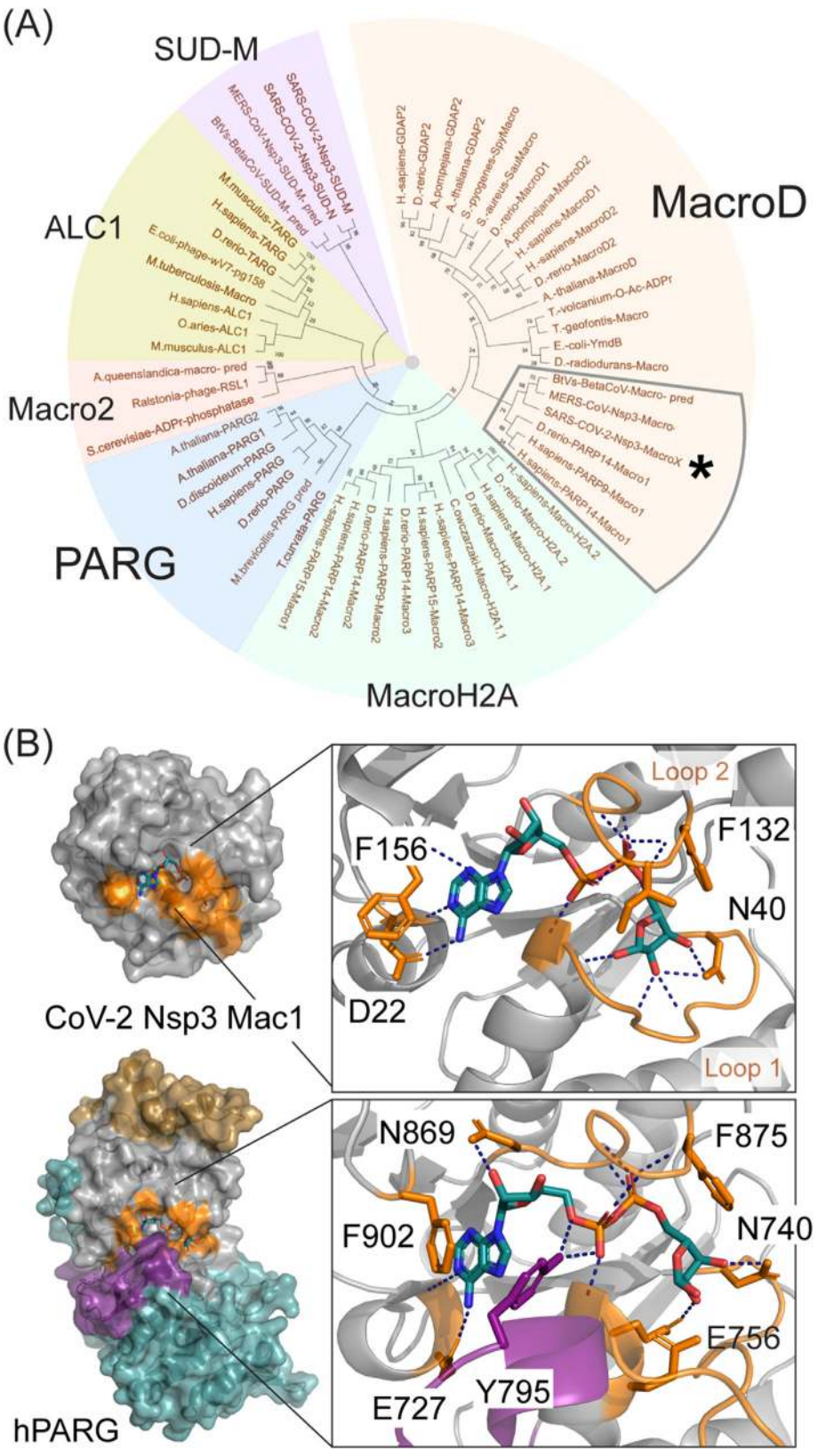

Fig. 2. CoV-2 Mac1 is a MacroD-like domain, but shares conserved active site architecture with PARG. (A) The phylogenetic tree of representative macrodomains forms six subfamilies. The CoV-2 Mac1 domain (indicated by an asterisk) is associated with the MacroD subfamily and shares closest homology with the N-terminal macrodomains of PARP9 and PARP14. (B) Domain and active site organization of CoV-2 Mac1 (PDB: 6W02) and PARG (PDB: 4B1H). The CoV-2 Mac1 domain forms a compact MacroD-like fold with Loops 1 and 2 coordinating the distal ribose through main chain hydrogen bonds. The macrodomain core of PARG is framed by an N-terminal accessory domain (teal) and helical C-terminus (gold), while a β-hairpin loop insert into the macrodomain wraps around to the active site to form a 'tyrosine clasp' (Y795, purple). Residues that contact ADP-ribose are highlighted in orange with hydrogen bonds (blue dashed lines) to the ADP-ribose ligand (teal).

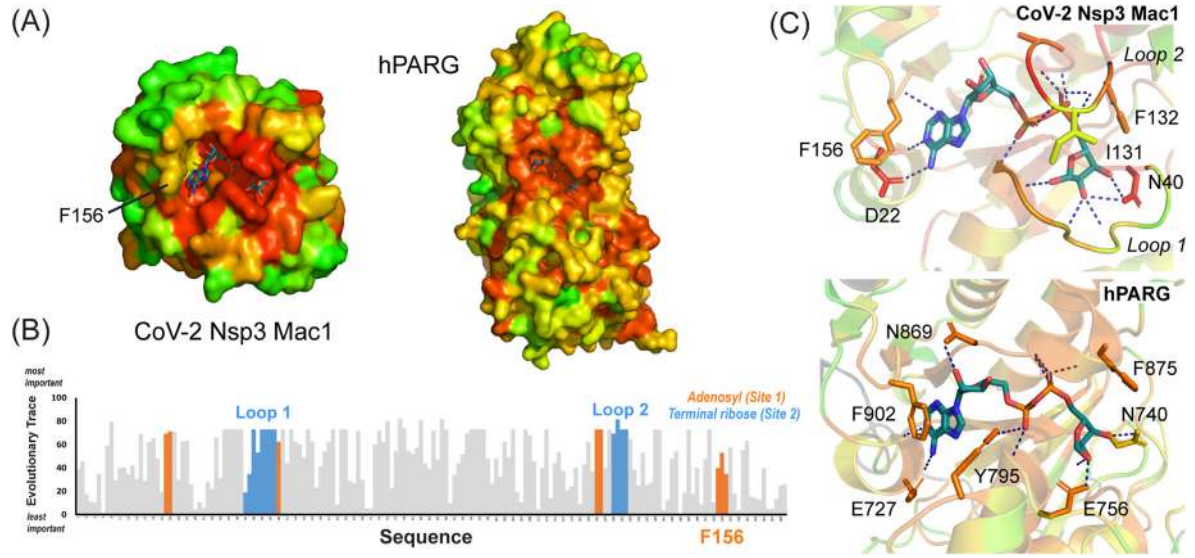

Fig. 3. CoV-2 Mac1 and PARG share critical adenosyl and ribose site residues. (A) Protein-specific ET analysis prioritizes CoV-2 Mac1 and PARG active sites (red/orange – high, green – low) as the location of greatest functional importance within the full-length proteins. (B) Plotting ET values (100 – most important, 0 - unimportant) against the CoV-2 Mac1 sequence reveals that adenosyl residue F156 is not as highly conserved among viral macrodomains. (C) ET values calculated across the entire macrodomain family highlight active site residues with the greatest shared functional conservation between CoV-2 Mac1 (F156, D22, N40, F132) and PARG (F902, E727, N740, F875).

the MES8-4 scaffold that substitutes a thiourea for the acyl sulfonamide linker, successfully crystallized with the CoV-2 Mac1 domain at 2.3 Å and 1.55 Å, respectively (Fig. 6, Table S3, Figs. S4, S5).

The backbone traces of these new Mac1 ligand complexes are highly similar to the MES crystal structure (PARG-345 C_α RMSD 0.169, PARG-329 C_α RMSD 0.358 Å) and closely mirror the conformation predicted by the MES8-4 computational studies, anchoring the methylxanthine head in the adenine pocket and the C8 morpholine in the terminal ribose pocket (Fig. 6C). Remarkably, the PARG-345 complex captures the major interactions observed in the original MES8-4 computational model (methylxanthine-I23, sulfonyl-Loop 2, morpholine-N40) (Fig. 6A and C). In contrast, the PARG-329 ligand primarily makes water-mediated contacts with the macrodomain and adopts a strained conformation to fit into the Mac1 active site (Fig. 6B). Of note, crystallographic temperature factors for residues defining the binding site remain low (20–50 $Å^2$) in both ligand-free and bound structures, indicating a comparatively rigid binding pocket and supporting the use of this experimentally observed active site architecture for inhibitor design efforts (Tainer et al., 1984).

Both Mac1 ligand linkers extend into and engage Loop 2. The PARG-329 thiourea makes two water-mediated contacts to the Loop 2 main chain, while the PARG-345 sulfonyl makes two backbone and one water-mediated contact with Loop 2, consistent with interactions observed in the MES8-4 model. While the Mac1 ligand linkers exhibit comparable binding interactions, the methylxanthine and morpholine groups display individual variations. The methylxanthine head is rotated 180° between PARG-329 and PARG-345. In this configuration, O3 of the PARG-345 methylxanthine directly hydrogen bonds with the I23 amide of the adenosyl pocket, while the PARG-329 methylxanthine remains engaged in water-mediated contacts. This variability in methylxanthine orientation echoes the variable adenine rotation of the Mac1/ADPr docking studies. F156, which has the potential to make π-stacking interactions with the methylxanthine, remains imperfectly aligned for direct π-to-π and edge-to-face contact. Further extension of the ligand linker could enable the methylxanthine to orient for direct stacking, providing one avenue for further ligand optimization.

The morpholine groups of each ligand also vary in their active site engagement. The PARG-345 morpholine assumes the low-energy chair conformation, allowing the terminal oxygen to hydrogen bond with the critical N40 side chain, as predicted by the MES8-4 computational modeling. In contrast, the PARG-329 morpholine oxygen is kinked away from N40 and hydrogen bonds with a water. The 3-atom spacing between the morpholine and thiourea appears to force the morpholine into the higher-energy conformation in order to fit into the rigid active site. This restricted positioning of the PARG-329 morpholine prevents optimal interaction with N40, which is expected to be a critical contact for ligand engagement.

Preliminary binding experiments between these ligands and the Mac1 domain by MST report micromolar affinity (PARG-329, Fig. S4; PARG-345, Fig. S5); however, ITC analysis fails to detect a robust interaction, suggesting further optimization of both ligands and binding assays is desirable. The prevalence of water-mediated contacts and strained ligand conformation observed in the PARG-329 crystal structure would be consistent with weaker engagement of the active site and reduced enthalpy generation, while also indicating strategies to improve direct hydrogen binding interactions. The prevalence of direct contacts between Mac1 and the PARG-345 ligand, as well as the more optimal ligand conformation suggests a more robust detection of binding affinity. A possible explanation for this discrepancy could be instability in the PARG-345 sulfonamide linker. Protonation of the morpholine nitrogen atom (pKa ~8.3) under assay conditions (pH 7.5–8.5) could facilitate β-elimination of the morpholine, depleting the intact ligand and producing weaker than expected Mac1 binding, indicating improvement of the linker would be fruitful.

These initial insights from MES8 crystal structures establish a viable framework for chemically targeting the Mac1 domain and show scope for continued improvement of the MES8 ligand scaffolds. Moreover, the similarity between the original MES8-4 computational model and crystallized PARG-345 ligand validates our application of rationale PARGi fragment design for constructing Mac1 inhibitors. Thus, the computational insights provided by PARGi screening and fragment design have provided an independent panel of Mac1 ligands for continued inhibitor development

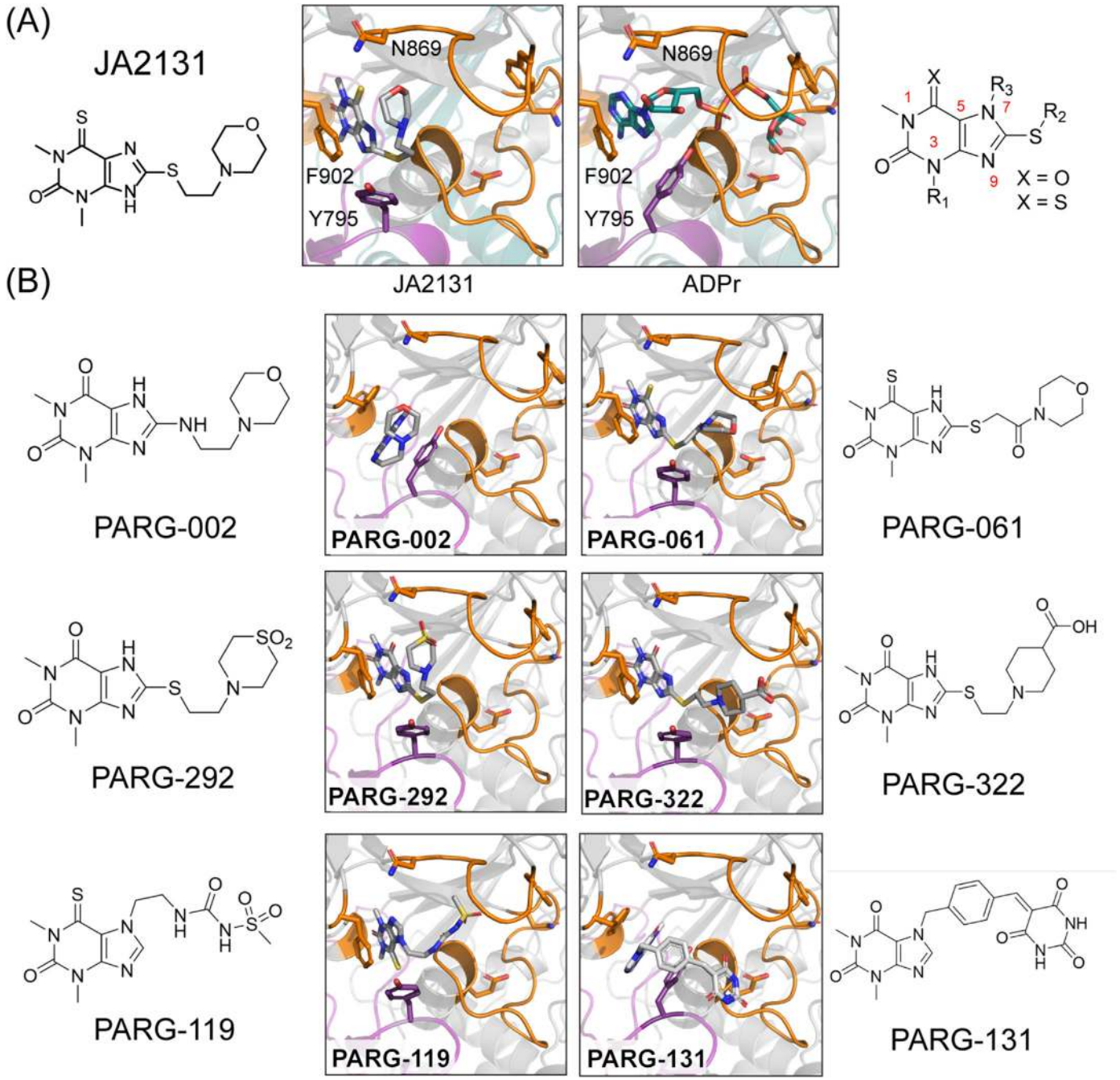

Fig. 4. The JA2131 PARGi derivative library engages with the PARG active site in a variety of ligand conformations. (A) The JA2131 lead PARGi inhibitor (gray) binds compactly in the adenosyl pocket of the PARG active site, compared to the elongated conformation of ADP-ribose (teal). (B) Crystal structures of PARG/inhibitor complexes from JA2131 derivatives modifying the C8 (PARG-002, PARG-061, PARG-292, PARG-322) or N7 (PARG-119, PARG-131) positions. Polder maps of ligands are displayed in Fig. S2.

guided by our prototypic Mac1-inhibitor complexes.

4. Discussion

The need for rapid and effective strategies to develop anti-viral therapies has emerged at the forefront of the COVID-19 pandemic. While the initial effectiveness of coronavirus vaccines is a huge advance, mutations which enhance viral infectivity and raise the possibility of vaccine escape variants are actively occurring (Plante et al., 2020), underscoring the need for ongoing research on new variants, coronaviruses, and therapies along with vaccines. Yet, there are currently no specific antiviral drugs to treat coronaviruses. Moreover, the possibility for viral reinfection makes the need for effective treatments even more immediate (Tillett et al., 2020). We therefore sought to develop a clear path for efficiently targeting CoV-2 Mac1 for drug discovery. Although fragment screening provides a productive structure-based discovery pathway (Wilson et al., 2020), recalibrating pre-existing drug development pipelines to target viral homologues provides an accelerated trajectory, avoiding the upfront time investment posed by fragment-based discovery and providing built-in design flexibility from pre-existing derivative optimization libraries. A similar homologue-

Table 2
MM/GBSA-ranked PARGi from CoV-2 Nps3 Mac1 virtual screening.

PARGi	MMGBSA ΔG (kcal/mol)	Chemotype	Anchor Point
ADPr	−74	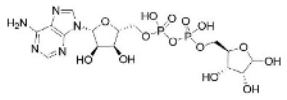	Native Ligand
PARG-025	−71	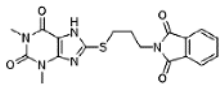	Adenosyl
PARG-025	−71	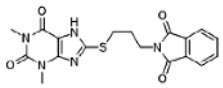	Adenosyl
PARG-129	−70	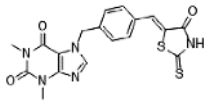	Adenosyl
PARG-305	−66	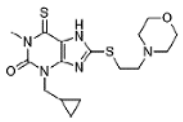	Ribose
PARG-038	−66	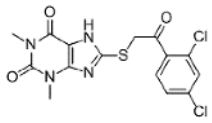	Ribose
PARG-129	−65	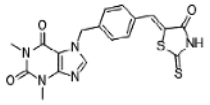	Adenosyl
PARG-257	−65	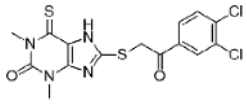	Ribose
PARG-108	−64	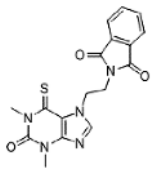	Ribose
PARG-120	−63	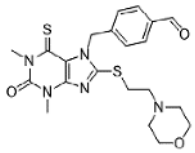	Ribose
PARG-066	−63	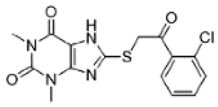	Ribose
PARG-066	−63	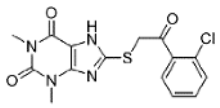	Ribose
PARG-033	−63	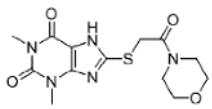	Ribose

Table 2 (*continued*)

PARGi	MMGBSA ΔG (kcal/mol)	Chemotype	Anchor Point
PARG-038	−61	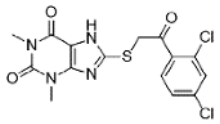	Ribose
PARG-252	−60	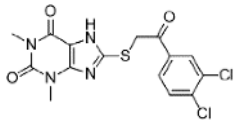	Ribose
PARG-258	−60	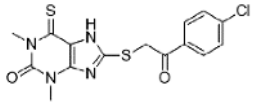	Ribose
PARG-013	−60	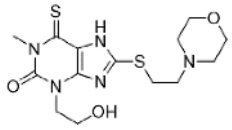	Ribose
PARG-272	−60	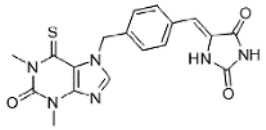	Adenosyl
PARG-025	−60	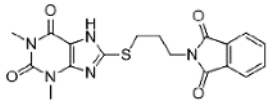	Adenosyl
PARG-120	−60	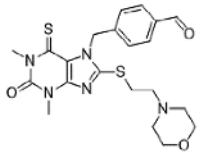	Ribose

based approach has been applied with success in the design of human MRE11 inhibitors using thermophilic Mre11 structural templates ('molecular avatars') (Moiani et al., 2018; Shibata et al., 2014).

Knowledge of active site architecture and flexibility is also critical for successful inhibitor development (Garcin et al., 2008; Houl et al., 2019). Relationships between active site motifs and functional regulation of ADP-ribosylation are well characterized among macrodomains from all domains of life, including bacterial and viral pathogens (Han et al., 1999; Han and Tainer, 2002; Jankevicius et al., 2013; Rack et al., 2020a). Here, we combined evolutionary, structural, and computational approaches to identify conserved macrodomain features and residues shared between DNA damage signaling factor PARG and the CoV-2 Mac1 active site. Similarities between their active sites support a strategy for using PARGi libraries and pipelines to develop CoV-2 Mac1 inhibitors. *In silico* screening of the methylxanthine JA2131 PARGi derivative library triages phenyl and morpholine derivatives for targeting the CoV-2 Mac1 distal ribose pocket, consistent with co-crystallization of MES in the same position. Reconfiguring the JA2131 linker to include electron-rich oxygen and sulfur atoms from sulfonyl and thiourea groups enabled the scaffold to simultaneously engage both adenosyl and ribose pockets while anchoring the linker with Loop 1 and 2 main chain contacts. These efforts have produced the novel Mac1 ligands, PARG-345 and PARG-329, which engage the Mac1 active site in a manner consistent with our computational analysis. This *in silico* framework has provided a lead scaffold for inhibitor development and is well positioned to capitalize upon experimental characterization of ligand inhibition using established methods from the PARGi development pipeline.

Effective CoV-2 Mac1 inhibitors are expected to lead to new biological understanding of COVID-19 pathogenesis and to critically needed antiviral drugs for vulnerable populations. Defining features of COVID-19 pathology point to disrupted innate antiviral defenses coupled with high inflammatory cytokine production (Blanco-Melo et al., 2020), where at-risk immunocompromised populations, such as cancer patients, have an increased likelihood of infection and severe events (Dai et al., 2020; Liang et al., 2020). The proposal of MARylated STAT1 as a putative CoV-2 Mac1 substrate (Claverie, 2020) presents an interesting hypothesis for testing the role of CoV-2 Mac1 in interferon regulation and in propagating the devastating effects of Cytokine Storm Syndrome, seen in severe COVID-19 patients (Zhang et al., 2020). Similarities shared between CoV-2 Mac1 and PARP9 and PARP14 macrodomains (Webb and Saad, 2020) also suggest hypotheses for investigating viral mimicry and interference in interferon production. These questions would be well served by specific and biologically effective CoV-2 Mac1 inhibitors. We expect our approach to provide a generalizable strategy for leveraging pre-existing inhibitor pipelines to create antiviral therapeutics, with particular relevance for COVID-19 and future coronavirus outbreaks.

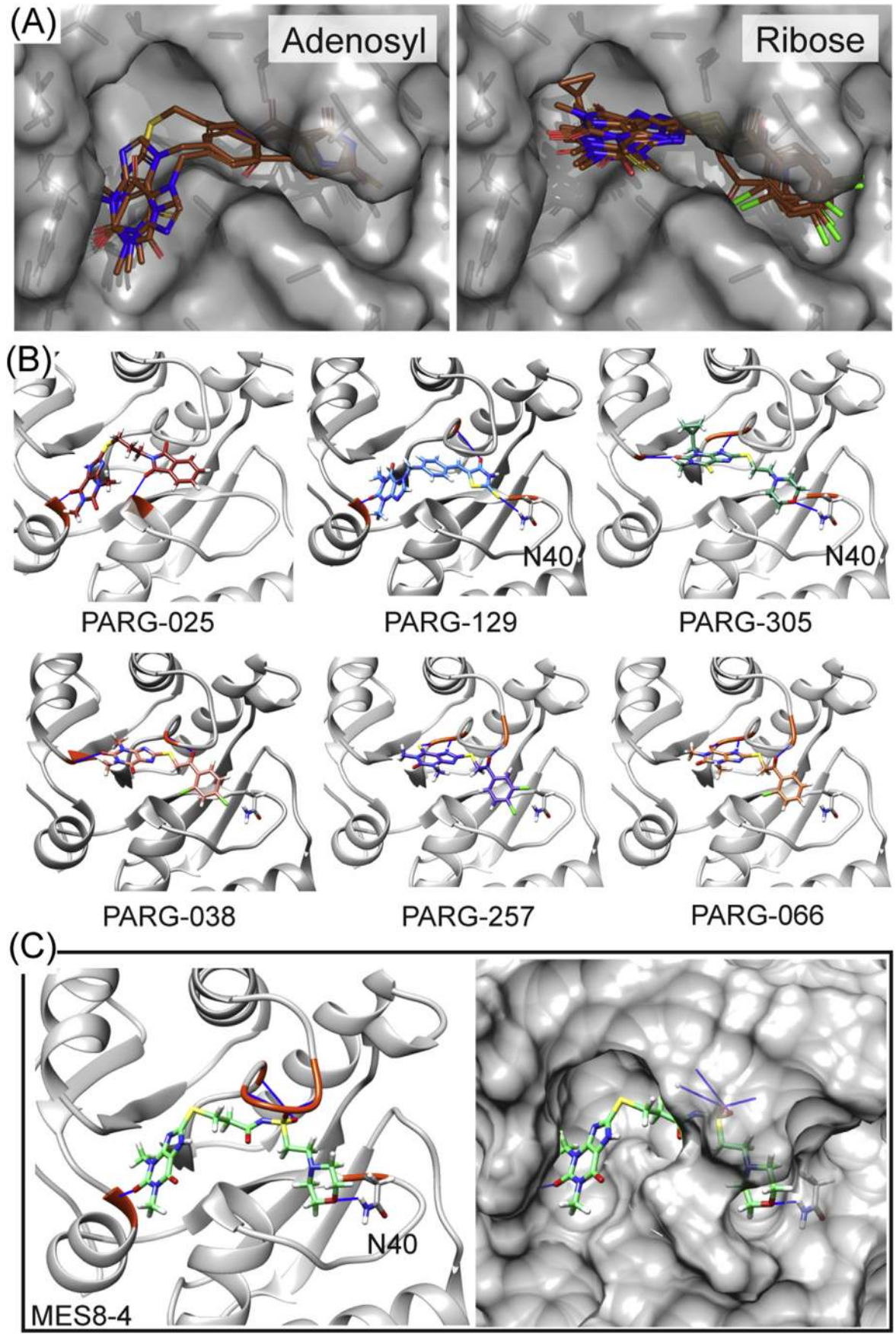
(A)
Adenosyl
Ribose
(B)
N40
N40
PARG-025
PARG-129
PARG-305
PARG-038
PARG-257
PARG-066
(C)
N40
MES8-4

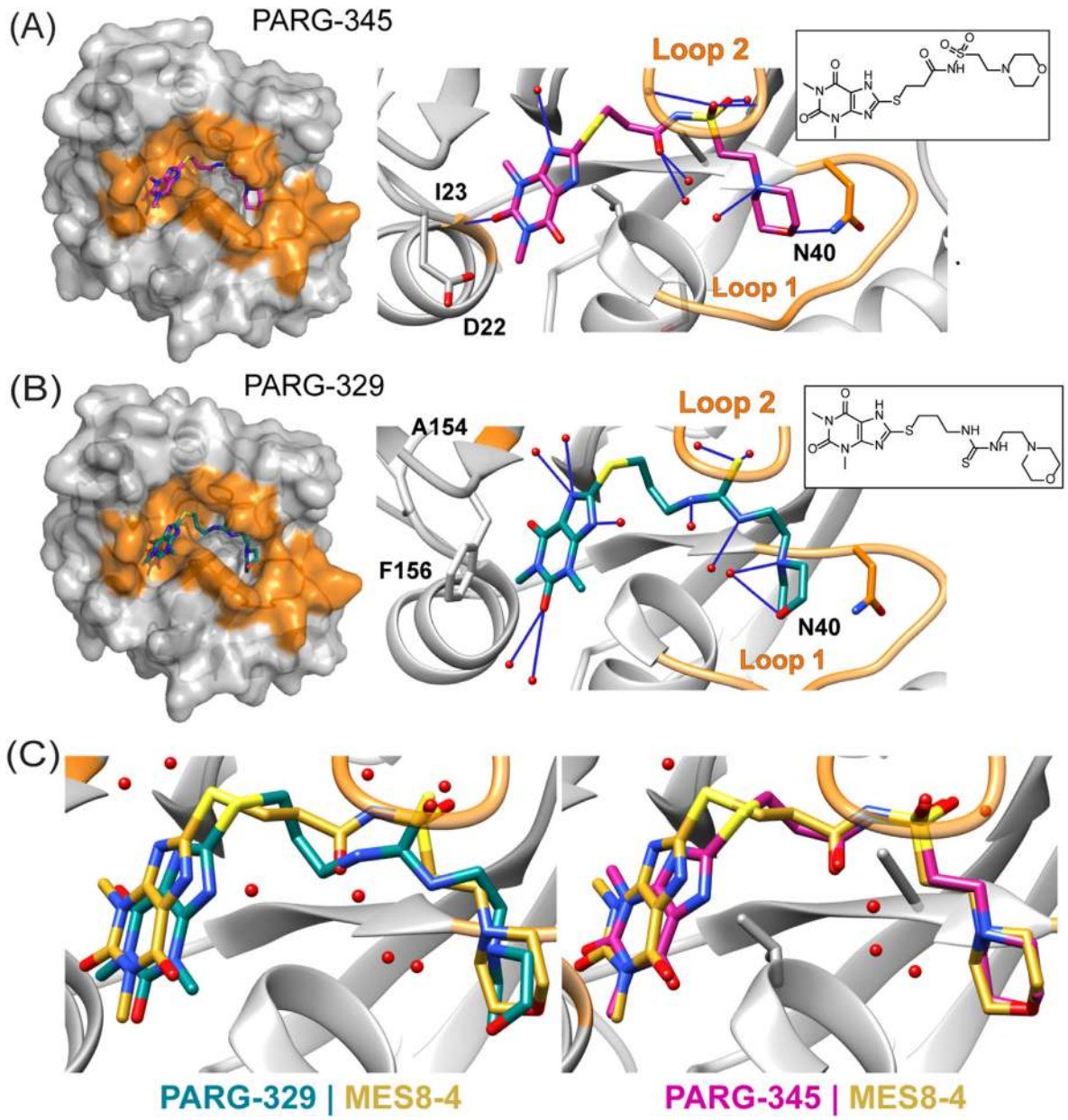

Fig. 6. PARGi-based Mac1 ligands PARG-345 (MES8-4) and PARG-329 bind the ADP-ribose active site. (A) Crystal structure of the Mac1/PARG-345 (MES8-4) complex. In addition to a main-chain contact (I23) at the xanthine head, the PARG-345 morpholine engages the critical N40 side-chain and makes direct backbone contacts with Loop 2 through the sulfonyl linker. See Fig. S5 for ligand Polder map. (B) Crystal structure of the Mac1/PARG-329 complex. The thiourea of PARG-329 engages Loop 2 through water-mediated contacts and adopts a strained morpholine conformation to fit into the active site. See Figure S4 for ligand Polder map. (C) Overlay of the original MES8-4 computational model (gold) with the crystallized PARG-329 (teal) and PARG-345 (magenta) ligands. MES8-4 successfully predicts the binding path and key contacts of these extended ligands in the Mac1 active site.

CRediT authorship contribution statement

Chris A. Brosey: Conceptualization, Investigation, Data curation, Formal analysis, Writing – original draft, Writing – review & editing, Visualization, Project administration. **Jerry H. Houl:** Investigation, Validation, Resources. **Panagiotis Katsonis:** Software, Formal analysis. **Lakshitha P.F. Balapiti-Modarage:** Resources. **Shobanbabu Bommagani:** Resources. **Andy Arvai:** Investigation, Data curation. **Davide Moiani:** Conceptualization, Methodology, Software. **Albino Bacolla:** Methodology, Software, Data curation. **Todd Link:** Validation, Resources. **Leslie S. Warden:** Resources. **Olivier Lichtarge:** Methodology, Supervision, Funding acquisition. **Darin E. Jones:** Conceptualization, Methodology, Resources, Writing – review & editing, Visualization, Supervision, Funding acquisition. **Zamal Ahmed:** Conceptualization, Investigation, Validation, Resources, Writing – review & editing, Funding acquisition. **John A. Tainer:** Conceptualization, Writing – review & editing, Supervision, Funding acquisition.

Fig. 5. *In silico* screening of JA2131 PARGi derivative library against CoV-2 Mac1. (A) PARGi poses associated into clusters anchored in the adenosyl pocket (left) or distal ribose pocket (right) of the CoV-2 Mac1 active site. (B) Selected PARGi poses from *in silico* screening show hydrogen bond contacts (solid blue lines) with N40, the Loop 2 main chain, or other residues (orange cartoon). (C) The computational model of CoV-2 Mac1 inhibitor MES8-4 shows the ligand bridging the adenosyl and distal ribose binding sites and making hydrogen bond contacts with conserved N40, the Loop 2 main chain, and I23 main chain.

Declaration of competing interest

The authors declare the following financial interests/personal relationships which may be considered as potential competing interests: C.A.B., D.M., D.E.J., Z.A., J.A.T are inventors on a patent application being submitted by M.D. Anderson Cancer Center that describes PARG inhibitors against COVID-19 macrodomain 1 (application pending).

Acknowledgements

This work was supported by National Institutes of Health (NIH) grant R01 CA200231 and a Robert A. Welch Chemistry Chair. D.J., L. P. F. B.-M., and S. B. are supported by NIH R01 CA200231. O. L. and P. K. are supported by AG061105 and NSF DBI-2032904. Retrieval of the *A. pompejana* macrodomain sequences used the Extreme Science and Engineering Discovery Environment (XSEDE) Bridges at the Pittsburgh Supercomputing Center through allocation MCB170053. Use of the Stanford Synchrotron Radiation Lightsource, SLAC National Acceleratory Laboratory, is supported by the U.S. Department of Energy, Office of Science, Office of Basic Energy Sciences under Contract No. DE-AC02-76SF00515. The SSRL Structural Molecular Biology Program is supported by the DOE Office of Biological and Environmental Research, and by the National Institutes of Health, National Institute of General Medical Sciences (P30 GM133894). This research used AMX (17-ID-1) and FMX (17-ID-2) of the National Synchrotron Light Source II, a U.S. Department of Energy (DOE) Office of Science User Facility operated for the DOE Office of Science by Brookhaven National Laboratory under Contract No. DE-SC0012704. The Center for BioMolecular Structure (CBMS) is primarily supported by the National Institutes of Health, National Institute of General Medical Sciences (NIGMS) through a Center Core P30 Grant (P30 GM133893), and by the DOE Office of Biological and Environmental Research (KP1605010). This work is based upon research conducted at the Northeastern Collaborative Access Team (NE-CAT) beamlines, which are funded by the National Institute of General Medical Sciences from the National Institutes of Health (P30 GM124165). This research used resources of the Advanced Photon Source, a U.S. Department of Energy (DOE) Office of Science User Facility operated for the DOE Office of Science by Argonne National Laboratory under Contract No. DE-AC02-06CH11357.

Appendix A. Supplementary data

Supplementary data to this article can be found online at https://doi.org/10.1016/j.pbiomolbio.2021.02.002.

GenBank deposition

The *A. pompejana* MacroD2 (gp30765.t1) and GDAP2 (g72977.t1) datasets generated during the current study are available in GenBank at http://www.ncbi.nlm.nih.gov/genbank/ with accession numbers MW349132 and MW383972.

PDB deposition

Structures of CoV-2 Mac1 and PARGi complexes have been deposited to the Protein Data Bank as follows: CoV-2 Mac1 (7KG3), CoV-2 Mac1/PARG-329 (7KXB), CoV-2 Mac1/PARG-345 (7LG7), PARG-002 (7KG1), PARG-061 (7KG8), PARG-119 (7KFP), PARG-131 (7KG0), PARG-292 (7KG7), PARG-322 (7KG6).

References

Abraham, R., McPherson, R.L., Dasovich, M., Badiee, M., Leung, A.K.L., Griffin, D.E., 2020. Both ADP-ribosyl-binding and hydrolase activities of the alphavirus nsP3 macrodomain affect neurovirulence in mice. mBio 11, 19–e03253.
Alhammad, Y.M.O., Fehr, A.R., 2020. The Viral Macrodomain Counters Host Antiviral ADP-Ribosylation, vol. 12. Viruses.
Altschul, S.F., Madden, T.L., Schäffer, A.A., Zhang, J., Zhang, Z., Miller, W., Lipman, D.J., 1997. Gapped BLAST and PSI-BLAST: a new generation of protein database search programs. Nucleic Acids Res. 25, 3389–3402.
Armougom, F., Moretti, S., Poirot, O., Audic, S., Dumas, P., Schaeli, B., Keduas, V., Notredame, C., 2006. Expresso: automatic incorporation of structural information in multiple sequence alignments using 3D-Coffee. Nucleic Acids Res. 34, W604–W608.
Bertrand, B., Stefan, L., Pirrotta, M., Monchaud, D., Bodio, E., Richard, P., Le Gendre, P., Warmerdam, E., de Jager, M.H., Groothuis, G.M., Picquet, M., Casini, A., 2014. Caffeine-based gold(I) N-heterocyclic carbenes as possible anticancer agents: synthesis and biological properties. Inorg. Chem. 53, 2296–2303.
Blanco-Melo, D., Nilsson-Payant, B.E., Liu, W.C., Uhl, S., Hoagland, D., Møller, R., Jordan, T.X., Oishi, K., Panis, M., Sachs, D., Wang, T.T., Schwartz, R.E., Lim, J.K., Albrecht, R.A., tenOever, B.R., 2020. Imbalanced host response to SARS-CoV-2 drives development of COVID-19. Cell 181, 1036–1045 e9.
Brosey, C.A., Ho, C., Long, W.Z., Singh, S., Burnett, K., Hura, G.L., Nix, J.C., Bowman, G.R., Ellenberger, T., Tainer, J.A., 2016. Defining NADH-driven allostery regulating apoptosis-inducing factor. Structure 24, 2067–2079.
Bunkoczi, G., Echols, N., McCoy, A.J., Oeffner, R.D., Adams, P.D., Read, R.J., 2013. Phaser.MRage: automated molecular replacement. Acta Crystallogr D Biol Crystallogr 69, 2276–2286.
Caprara, G., Prosperini, E., Piccolo, V., Sigismondo, G., Melacarne, A., Cuomo, A., Boothby, M., Rescigno, M., Bonaldi, T., Natoli, G., 2018. PARP14 controls the nuclear accumulation of a subset of type I IFN-inducible proteins. J. Immunol. 200, 2439–2454.
Chen, S.-H., Yu, X., 2019. Targeting dePARylation selectively suppresses DNA repair–defective and PARP inhibitor–resistant malignancies. Science Advances 5, eaav4340.
Claverie, J.M., 2020. A putative role of de-mono-ADP-ribosylation of STAT1 by the SARS-CoV-2 Nsp3 protein in the cytokine Storm syndrome of COVID-19. Viruses 12.
Dai, M., Liu, D., Liu, M., Zhou, F., Li, G., Chen, Z., Zhang, Z., You, H., Wu, M., Zheng, Q., Xiong, Y., Xiong, H., Wang, C., Chen, C., Xiong, F., Zhang, Y., Peng, Y., Ge, S., Zhen, B., Yu, T., Wang, L., Wang, H., Liu, Y., Chen, Y., Mei, J., Gao, X., Li, Z., Gan, L., He, C., Li, Z., Shi, Y., Qi, Y., Yang, J., Tenen, D.G., Chai, L., Mucci, L.A., Santillana, M., Cai, H., 2020. Patients with cancer appear more vulnerable to SARS-CoV-2: a multicenter study during the COVID-19 outbreak. Canc. Discov. 10, 783–791.
Eckelmann, B.J., Bacolla, A., Wang, H., Ye, Z., Guerrero, E.N., Jiang, W., El-Zein, R., Hegde, M.L., Tomkinson, A.E., Tainer, J.A., Mitra, S., 2020. XRCC1 promotes replication restart, nascent fork degradation and mutagenic DNA repair in BRCA2-deficient cells. NAR Cancer 2 zcaa013.
Edgar, R.C., 2004. MUSCLE: multiple sequence alignment with high accuracy and high throughput. Nucleic Acids Res. 32, 1792–1797.
Elliott, T., Slowey, A., Ye, Y., Conway, S., 2012. The use of phosphate bioisosteres in medicinal chemistry and chemical biology. MedChemComm 3.
Emsley, P., Cowtan, K., 2004. Coot: model-building tools for molecular graphics. Acta Crystallogr D Biol Crystallogr 60, 2126–2132.
Fehr, A.R., Athmer, J., Channappanavar, R., Phillips, J.M., Meyerholz, D.K., Perlman, S., 2015. The nsp3 macrodomain promotes virulence in mice with coronavirus-induced encephalitis. J. Virol. 89, 1523–1536.
Fehr, A.R., Channappanavar, R., Jankevicius, G., Fett, C., Zhao, J., Athmer, J., Meyerholz, D.K., Ahel, I., Perlman, S., 2016. The conserved coronavirus macrodomain promotes virulence and suppresses the innate immune response during severe acute respiratory syndrome coronavirus infection. mBio 7.
Fehr, A.R., Jankevicius, G., Ahel, I., Perlman, S., 2018. Viral macrodomains: unique mediators of viral replication and pathogenesis. Trends Microbiol. 26, 598–610.
Felsenstein, J., 1985. Confidence Limits on Phylognies: an Approach Using the Bootstrap Evolution, pp. 783–791.
Fraser, J.S., 2020. Identifying New Ligands for the SARS-CoV-2 Macrodomain by Fragment Screening and Multi-Temperature Crystallography (Version 1.0). Zenodo.
Frick, D.N., Virdi, R.S., Vuksanovic, N., Dahal, N., Silvaggi, N.R., 2020. Molecular basis for ADP-ribose binding to the Mac1 domain of SARS-CoV-2 nsp3. Biochemistry 59, 2608–2615.
Garcin, E.D., Arvai, A.S., Rosenfeld, R.J., Kroeger, M.D., Crane, B.R., Andersson, G., Andrews, G., Hamley, P.J., Mallinder, P.R., Nicholls, D.J., St-Gallay, S.A., Tinker, A.C., Gensmantel, N.P., Mete, A., Cheshire, D.R., Connolly, S., Stuehr, D.J., Aberg, A., Wallace, A.V., Tainer, J.A., Getzoff, E.D., 2008. Anchored plasticity opens doors for selective inhibitor design in nitric oxide synthase. Nat. Chem. Biol. 4, 700–707.
Grunewald, M.E., Chen, Y., Kuny, C., Maejima, T., Lease, R., Ferraris, D., Aikawa, M., Sullivan, C.S., Perlman, S., Fehr, A.R., 2019. The coronavirus macrodomain is required to prevent PARP-mediated inhibition of virus replication and enhancement of IFN expression. PLoS Pathog. 15, e1007756.
Guan, W.-j., Ni, Z.-y., Hu, Y., Liang, W.-h., Ou, C.-q., He, J.-x., Liu, L., Shan, H., Lei, C.-l., Hui, D.S.C., Du, B., Li, L.-j., Zeng, G., Yuen, K.-Y., Chen, R.-c., Tang, C.-l., Wang, T., Chen, P.-y., Xiang, J., Li, S.-y., Wang, J.-l., Liang, Z.-j., Peng, Y.-x., Wei, L., Liu, Y.,

Hu, Y.-h., Peng, P., Wang, J.-m., Liu, J.-y., Chen, Z., Li, G., Zheng, Z.-j., Qiu, S.-q., Luo, J., Ye, C.-j., Zhu, S.-y., Zhong, N.-s., 2020. Clinical characteristics of coronavirus disease 2019 in China. N. Engl. J. Med. 382, 1708–1720.
Han, S., Craig, J.A., Putnam, C.D., Carozzi, N.B., Tainer, J.A., 1999. Evolution and mechanism from structures of an ADP-ribosylating toxin and NAD complex. Nat. Struct. Biol. 6, 932–936.
Han, S., Tainer, J.A., 2002. The ARTT motif and a unified structural understanding of substrate recognition in ADP-ribosylating bacterial toxins and eukaryotic ADP-ribosyltransferases. Int J Med Microbiol 291, 523–529.
Hisham, M., Youssif, B.G.M., Osman, E.E.A., Hayallah, A.M., Abdel-Aziz, M., 2019. Synthesis and biological evaluation of novel xanthine derivatives as potential apoptotic antitumor agents. Eur. J. Med. Chem. 176, 117–128.
Holder, T., Basquin, C., Ebert, J., Randel, N., Jollivet, D., Conti, E., Jékely, G., Bono, F., 2013. Deep transcriptome-sequencing and proteome analysis of the hydrothermal vent annelid Alvinella pompejana identifies the CvP-bias as a robust measure of eukaryotic thermostability. Biol. Direct 8, 2.
Houl, J.H., Ye, Z., Brosey, C.A., Balapiti-Modarage, L.P.F., Namjoshi, S., Bacolla, A., Laverty, D., Walker, B.L., Pourfarjam, Y., Warden, L.S., Babu Chinnam, N., Moiani, D., Stegeman, R.A., Chen, M.-K., Hung, M.-C., Nagel, Z.D., Ellenberger, T., Kim, I.-K., Jones, D.E., Ahmed, Z., Tainer, J.A., 2019. Selective small molecule PARG inhibitor causes replication fork stalling and cancer cell death. Nat. Commun. 10, 5654, 5654.
Iwata, H., Goettsch, C., Sharma, A., Ricchiuto, P., Goh, W.W., Halu, A., Yamada, I., Yoshida, H., Hara, T., Wei, M., Inoue, N., Fukuda, D., Mojcher, A., Mattson, P.C., Barabasi, A.L., Boothby, M., Aikawa, E., Singh, S.A., Aikawa, M., 2016. PARP9 and PARP14 cross-regulate macrophage activation via STAT1 ADP-ribosylation. Nat. Commun. 7, 12849.
Jankevicius, G., Hassler, M., Golia, B., Rybin, V., Zacharias, M., Timinszky, G., Ladurner, A.G., 2013. A family of macrodomain proteins reverses cellular mono-ADP-ribosylation. Nat. Struct. Mol. Biol. 20, 508–514.
Kabsch, W., 2010. Xds. Acta Crystallogr D Biol Crystallogr 66, 125–132.
Kim, I.-K., Kiefer, J.R., Ho, C.M.W., Stegeman, R.A., Classen, S., Tainer, J.A., Ellenberger, T., 2012. Structure of mammalian poly(ADP-ribose) glycohydrolase reveals a flexible tyrosine clasp as a substrate-binding element. Nat. Struct. Mol. Biol. 19, 653–656.
Kumar, S., Stecher, G., Li, M., Knyaz, C., Tamura, K., 2018. Mega X: molecular evolutionary genetics analysis across computing platforms. Mol. Biol. Evol. 35, 1547–1549.
Lam, T.T.-Y., Jia, N., Zhang, Y.-W., Shum, M.H.-H., Jiang, J.-F., Zhu, H.-C., Tong, Y.-G., Shi, Y.-X., Ni, X.-B., Liao, Y.-S., Li, W.-J., Jiang, B.-G., Wei, W., Yuan, T.-T., Zheng, K., Cui, X.-M., Li, J., Pei, G.-Q., Qiang, X., Cheung, W.Y.-M., Li, L.-F., Sun, F.-F., Qin, S., Huang, J.-C., Leung, G.M., Holmes, E.C., Hu, Y.-L., Guan, Y., Cao, W.-C., 2020. Identifying SARS-CoV-2-related coronaviruses in Malayan pangolins. Nature 583, 282–285.
Lambrecht, M.J., Brichacek, M., Barkauskaite, E., Ariza, A., Ahel, I., Hergenrother, P.J., 2015. Synthesis of dimeric ADP-ribose and its structure with human poly(ADP-ribose) glycohydrolase. J. Am. Chem. Soc. 137, 3558–3564.
Liang, W., Guan, W., Chen, R., Wang, W., Li, J., Xu, K., Li, C., Ai, Q., Lu, W., Liang, H., Li, S., He, J., 2020. Cancer patients in SARS-CoV-2 infection: a nationwide analysis in China. Lancet Oncol. 21, 335–337.
Lichtarge, O., Bourne, H.R., Cohen, F.E., 1996. An evolutionary trace method defines binding surfaces common to protein families. J. Mol. Biol. 257, 342–358.
Liebschner, D., Afonine, P.V., Baker, M.L., Bunkoczi, G., Chen, V.B., Croll, T.I., Hintze, B., Hung, L.W., Jain, S., McCoy, A.J., Moriarty, N.W., Oeffner, R.D., Poon, B.K., Prisant, M.G., Read, R.J., Richardson, J.S., Richardson, D.C., Sammito, M.D., Sobolev, O.V., Stockwell, D.H., Terwilliger, T.C., Urzhumtsev, A.G., Videau, L.L., Williams, C.J., Adams, P.D., 2019. Macromolecular structure determination using X-rays, neutrons and electrons: recent developments in Phenix. Acta Crystallogr D Struct Biol 75, 861–877.
Liebschner, D., Afonine, P.V., Moriarty, N.W., Poon, B.K., Sobolev, O.V., Terwilliger, T.C., Adams, P.D., 2017. Polder maps: improving OMIT maps by excluding bulk solvent. Acta Crystallogr D Struct Biol 73, 148–157.
Lin, M.H., Chang, S.C., Chiu, Y.C., Jiang, B.C., Wu, T.H., Hsu, C.H., 2020. Structural, biophysical, and biochemical elucidation of the SARS-CoV-2 nonstructural protein 3 macro domain. ACS Infect. Dis. 6, 2970–2978.
Lua, R.C., Lichtarge, O., 2010. PyETV: a PyMOL evolutionary trace viewer to analyze functional site predictions in protein complexes. Bioinformatics 26, 2981–2982.
McPherson, R.L., Abraham, R., Sreekumar, E., Ong, S.-E., Cheng, S.-J., Baxter, V.K., Kistemaker, H.A.V., Filippov, D.V., Griffin, D.E., Leung, A.K.L., 2017. ADP-ribosylhydrolase activity of Chikungunya virus macrodomain is critical for virus replication and virulence. Proc. Natl. Acad. Sci. Unit. States Am. 114, 1666–1671.
Michalska, K., Kim, Y., Jedrzejczak, R., Maltseva, N.I., Stols, L., Endres, M., Joachimiak, A., 2020. Crystal structures of SARS-CoV-2 ADP-ribose phosphatase: from the apo form to ligand complexes. IUCrJ 7, 814–824.
Mihalek, I., Res, I., Lichtarge, O., 2004. A family of evolution-entropy hybrid methods for ranking protein residues by importance. J. Mol. Biol. 336, 1265–1282.
Moiani, D., Ronato, D.A., Brosey, C.A., Arvai, A.S., Syed, A., Masson, J.Y., Petricci, E., Tainer, J.A., 2018. Targeting allostery with avatars to design inhibitors assessed by cell activity: dissecting MRE11 endo- and exonuclease activities. Methods Enzymol. 601, 205–241.
Moriarty, N.W., Grosse-Kunstleve, R.W., Adams, P.D., 2009. Electronic Ligand Builder and Optimization Workbench (eLBOW): a tool for ligand coordinate and restraint generation. Acta Crystallogr D Biol Crystallogr 65, 1074–1080.
Morin, A., Eisenbraun, B., Key, J., Sanschagrin, P.C., Timony, M.A., Ottaviano, M., Sliz, P., 2013. Collaboration gets the most out of software. Elife 2, e01456.
Nei, M.a.K.S., 2000. Molecular Evolution and Phylogenetics. Oxford University Press, New York.
Notredame, C., Higgins, D.G., Heringa, J., 2000. T-Coffee: a novel method for fast and accurate multiple sequence alignment. J. Mol. Biol. 302, 205–217.
Omolo, C.A., Soni, N., Fasiku, V.O., Mackraj, I., Govender, T., 2020. Update on therapeutic approaches and emerging therapies for SARS-CoV-2 virus. Eur. J. Pharmacol. 883, 173348.
Pettersen, E.F., Goddard, T.D., Huang, C.C., Couch, G.S., Greenblatt, D.M., Meng, E.C., Ferrin, T.E., 2004. UCSF Chimera–a visualization system for exploratory research and analysis. J. Comput. Chem. 25, 1605–1612.
Plante, J.A., Liu, Y., Liu, J., Xia, H., Johnson, B.A., Lokugamage, K.G., Zhang, X., Muruato, A.E., Zou, J., Fontes-Garfias, C.R., Mirchandani, D., Scharton, D., Bilello, J.P., Ku, Z., An, Z., Kalveram, B., Freiberg, A.N., Menachery, V.D., Xie, X., Plante, K.S., Weaver, S.C., Shi, P.Y., 2020. Spike mutation D614G alters SARS-CoV-2 fitness. Nature. https://doi.org/10.1038/s41586-020-2895-3.
Pourfarjam, Y., Kasson, S., Tran, L., Ho, C., Lim, S., Kim, I.-K., 2020. PARG has a robust endo-glycohydrolase activity that releases protein-free poly(ADP-ribose) chains. Biochem. Biophys. Res. Commun. 527, 818–823.
Pruitt, K.D., Tatusova, T., Maglott, D.R., 2007. NCBI reference sequences (RefSeq): a curated non-redundant sequence database of genomes, transcripts and proteins. Nucleic Acids Res. 35, D61–D65.
Rack, J.G.M., Palazzo, L., Ahel, I., 2020a. (ADP-ribosyl)hydrolases: structure, function, and biology. Genes Dev. 34, 263–284.
Rack, J.G.M., Perina, D., Ahel, I., 2016. Macrodomains: structure, function, evolution, and catalytic activities. Annu. Rev. Biochem. 85, 431–454.
Rack, J.G.M., Zorzini, V., Zhu, Z., Schuller, M., Ahel, D., Ahel, I., 2020b. Viral macrodomains: a structural and evolutionary assessment of the pharmacological potential. Open Biol 10, 200237.
Russi, S., Song, J., McPhillips, S.E., Cohen, A.E., 2016. The Stanford Automated Mounter: pushing the limits of sample exchange at the SSRL macromolecular crystallography beamlines. J. Appl. Crystallogr. 49, 622–626.
Saitou, N., Nei, M., 1987. The neighbor-joining method: a new method for reconstructing phylogenetic trees. Mol. Biol. Evol. 4, 406–425.
Seidel, S.A., Dijkman, P.M., Lea, W.A., van den Bogaart, G., Jerabek-Willemsen, M., Lazic, A., Joseph, J.S., Srinivasan, P., Baaske, P., Simeonov, A., Katritch, I., Melo, F.A., Ladbury, J.E., Schreiber, G., Watts, A., Braun, D., Duhr, S., 2013. Microscale thermophoresis quantifies biomolecular interactions under previously challenging conditions. Methods 59, 301–315.
Shibata, A., Moiani, D., Arvai, A.S., Perry, J., Harding, S.M., Genois, M.M., Maity, R., van Rossum-Fikkert, S., Kertokalio, A., Romoli, F., Ismail, A., Ismalaj, E., Petricci, E., Neale, M.J., Bristow, R.G., Masson, J.Y., Wyman, C., Jeggo, P.A., Tainer, J.A., 2014. DNA double-strand break repair pathway choice is directed by distinct MRE11 nuclease activities. Mol. Cell. 53, 7–18.
Shin, D.S., Didonato, M., Barondeau, D.P., Hura, G.L., Hitomi, C., Berglund, J.A., Getzoff, E.D., Cary, S.C., Tainer, J.A., 2009. Superoxide dismutase from the eukaryotic thermophile Alvinella pompejana: structures, stability, mechanism, and insights into amyotrophic lateral sclerosis. J. Mol. Biol. 385, 1534–1555.
Shyr, Z.A., Gorshkov, K., Chen, C.Z., Zheng, W., 2020. Drug discovery strategies for SARS-CoV-2. J. Pharmacol. Exp. Therapeut. 375, 127–138. JPET-MR-2020-000123.
Slade, D., 2020. PARP and PARG inhibitors in cancer treatment. Genes Dev. 34, 360–394.
Slade, D., Dunstan, M.S., Barkauskaite, E., Weston, R., Lafite, P., Dixon, N., Ahel, M., Leys, D., Ahel, I., 2011. The structure and catalytic mechanism of a poly(ADP-ribose) glycohydrolase. Nature 477, 616–620.
Soltis, S.M., Cohen, A.E., Deacon, A., Eriksson, T., González, A., McPhillips, S., Chui, H., Dunten, P., Hollenbeck, M., Mathews, I., Miller, M., Moorhead, P., Phizackerley, R.P., Smith, C., Song, J., van dem Bedem, H., Ellis, P., Kuhn, P., McPhillips, T., Sauter, N., Sharp, K., Tsyba, I., Wolf, G., 2008. New paradigm for macromolecular crystallography experiments at SSRL: automated crystal screening and remote data collection. Acta Crystallogr D Biol Crystallogr 64, 1210–1221.
Stanke, M., Morgenstern, B., 2005. AUGUSTUS: a web server for gene prediction in eukaryotes that allows user-defined constraints. Nucleic Acids Res. 33, W465–W467.
Stecher, G., Tamura, K., Kumar, S., 2020. Molecular evolutionary genetics analysis (MEGA) for macOS. Mol. Biol. Evol. 37, 1237–1239.
Suzek, B.E., Wang, Y., Huang, H., McGarvey, P.B., Wu, C.H., 2015. UniRef clusters: a comprehensive and scalable alternative for improving sequence similarity searches. Bioinformatics 31, 926–932.
Syed, A., Tainer, J.A., 2018. The MRE11-RAD50-NBS1 complex conducts the orchestration of damage signaling and outcomes to stress in DNA replication and repair. Annu. Rev. Biochem. 87, 263–294.
Tainer, J.A., Getzoff, E.D., Alexander, H., Houghten, R.A., Olson, A.J., Lerner, R.A., Hendrickson, W.A., 1984. The reactivity of anti-peptide antibodies is a function of the atomic mobility of sites in a protein. Nature 312, 127–134.
Tillett, R.L., Sevinkay, J.R., Hartley, P.D., Kerwin, H., Crawford, N., Gorzalski, A., Laverdure, C., Verma, S.C., Rossetto, C.C., JAckson, D., Farrell, M.J., Van Hooser, S., Pandori, M., 2020. Genomic evidence for reinfection with SARS-CoV-2: a case study. Lancet Infect. Dis. 21, P52–P58.
Touret, F., Gilles, M., Barral, K., Nougairède, A., van Helden, J., Decroly, E., de Lamballerie, X., Coutard, B., 2020. In vitro screening of a FDA approved chemical library reveals potential inhibitors of SARS-CoV-2 replication. Sci. Rep. 10, 13093.
Tucker, J.A., Bennett, N., Brassington, C., Durant, S.T., Hassall, G., Holdgate, G.,

McAlister, M., Nissink, J.W.M., Truman, C., Watson, M., 2012. Structures of the human poly (ADP-ribose) glycohydrolase catalytic domain confirm catalytic mechanism and explain inhibition by ADP-HPD derivatives. PloS One 7, e50889 e50889.

Wang, Y., Kim, N.S., Haince, J.F., Kang, H.C., David, K.K., Andrabi, S.A., Poirier, G.G., Dawson, V.L., Dawson, T.M., 2011. Poly(ADP-ribose) (PAR) binding to apoptosis-inducing factor is critical for PAR polymerase-1-dependent cell death (parthanatos). Sci. Signal. 4, ra20.

Webb, T.E., Saad, R., 2020. Sequence homology between human PARP14 and the SARS-CoV-2 ADP ribose 1'-phosphatase. Immunol. Lett. 224, 38–39.

Wilson 3rd, D.M., Deacon, A.M., Duncton, M.A.J., Pellicena, P., Georgiadis, M.M., Yeh, A.P., Arvai, A.S., Moiani, D., Tainer, J.A., Das, D., 2020. Fragment- and structure-based drug discovery for developing therapeutic agents targeting the DNA Damage Response. Prog. Biophys. Mol. Biol. https://doi.org/10.1016/j.pbiomolbio.2020.10.005. In press.

Winn, M.D., Ballard, C.C., Cowtan, K.D., Dodson, E.J., Emsley, P., Evans, P.R., Keegan, R.M., Krissinel, E.B., Leslie, A.G., McCoy, A., McNicholas, S.J., Murshudov, G.N., Pannu, N.S., Potterton, E.A., Powell, H.R., Read, R.J., Vagin, A., Wilson, K.S., 2011. Overview of the CCP4 suite and current developments. Acta Crystallogr D Biol Crystallogr 67, 235–242.

Zandarashvili, L., Langelier, M.F., Velagapudi, U.K., Hancock, M.A., Steffen, J.D., Billur, R., Hannan, Z.M., Wicks, A.J., Krastev, D.B., Pettitt, S.J., Lord, C.J., Talele, T.T., Pascal, J.M., Black, B.E., 2020. Structural basis for allosteric PARP-1 retention on DNA breaks. Science 368.

Zhang, C., Wu, Z., Li, J.W., Zhao, H., Wang, G.Q., 2020. Cytokine release syndrome in severe COVID-19: interleukin-6 receptor antagonist tocilizumab may be the key to reduce mortality. Int. J. Antimicrob. Agents 55, 105954.

Zhang, Y., Mao, D., Roswit, W.T., Jin, X., Patel, A.C., Patel, D.A., Agapov, E., Wang, Z., Tidwell, R.M., Atkinson, J.J., Huang, G., McCarthy, R., Yu, J., Yun, N.E., Paessler, S., Lawson, T.G., Omattage, N.S., Brett, T.J., Holtzman, M.J., 2015. PARP9-DTX3L ubiquitin ligase targets host histone H2BJ and viral 3C protease to enhance interferon signaling and control viral infection. Nat. Immunol. 16, 1215–1227.

Zhou, P., Yang, X.-L., Wang, X.-G., Hu, B., Zhang, L., Zhang, W., Si, H.-R., Zhu, Y., Li, B., Huang, C.-L., Chen, H.-D., Chen, J., Luo, Y., Guo, H., Jiang, R.-D., Liu, M.-Q., Chen, Y., Shen, X.-R., Wang, X., Zheng, X.-S., Zhao, K., Chen, Q.-J., Deng, F., Liu, L.-L., Yan, B., Zhan, F.-X., Wang, Y.-Y., Xiao, G.-F., Shi, Z.-L., 2020. A pneumonia outbreak associated with a new coronavirus of probable bat origin. Nature 579, 270–273.